PNAS RESEARCH ARTICLE | CHEMISTRY

Promote electroreduction of CO_2 via catalyst valence state manipulation by surface-capping ligand

Yilin Zhao[a,1], Xiaoqing Liu[b,1], Jingyi Chen[a,1], Junmei Chen[a], Jiayi Chen[a], Lei Fan[a], Haozhou Yang[a], Shibo Xi[c], Lei Shen[b], and Lei Wang[a,2]

Edited by Alexis Bell, University of California, Berkeley, CA; received October 23, 2022; accepted April 10, 2023

Electrochemical CO_2 reduction provides a potential means for synthesizing value-added chemicals over the near equilibrium potential regime, i.e., formate production on Pd-based catalysts. However, the activity of Pd catalysts has been largely plagued by the potential-depended deactivation pathways (e.g., α-PdH to β-PdH phase transition, CO poisoning), limiting the formate production to a narrow potential window of 0 V to −0.25 V vs. reversible hydrogen electrode (RHE). Herein, we discovered that the Pd surface capped with polyvinylpyrrolidone (PVP) ligand exhibits effective resistance to the potential-depended deactivations and can catalyze formate production at a much extended potential window (beyond −0.7 V vs. RHE) with significantly improved activity (~14-times enhancement at −0.4 V vs. RHE) compared to that of the pristine Pd surface. Combined results from physical and electrochemical characterizations, kinetic analysis, and first-principle simulations suggest that the PVP capping ligand can effectively stabilize the high-valence-state Pd species ($Pd^{\delta+}$) resulted from the catalyst synthesis and pretreatments, and these $Pd^{\delta+}$ species are responsible for the inhibited phase transition from α-PdH to β-PdH, and the suppression of CO and H_2 formation. The present study confers a desired catalyst design principle, introducing positive charges into Pd-based electrocatalyst to enable efficient and stable CO_2 to formate conversion.

electrocatalysis | CO_2 reduction | formate | capping ligand | valence state

Electrochemical CO_2 reduction (CO_2R) offers an opportunity to turn the waste carbon into value-added chemicals/fuels and further to mitigate the pressing carbon emission issues (1–4). A variety of products ranging from single- to multiple-carbon oxygenates and hydrocarbons can be obtained from CO_2R (5–13). Therein, two-electron products such as formate ($HCOO^-$, or formic acid HCOOH in acidic media) have attracted particular interest, as it shows promising chance to achieve near-term economic feasibility (14, 15). Several electrocatalyst candidates, e.g., Sn-based (16–19), In-based (18), Bi-based (19–21), N-doped carbon electrode materials (22–24), etc., have shown encouraging selectivity toward formate; however, the large overpotentials required remains a major challenge for their practical implementations. In contrast, Pd-based electrocatalysts have demonstrated appreciable activity and superior selectivity for formate production at regions of low to even zero overpotentials (25–32). However, Pd-based catalysts deactivate quickly for formate production with the increase of overpotential, i.e., typically formate selectivity drops from >90% to <20% from near 0 V vs. RHE (reversible hydrogen electrode) to ~−0.4 V vs. RHE, together with sharp decrease in formate formation current-density (25, 33). This potential-dependent deactivation is closely associated with the phase transition of the Pd-sites and CO poisoning (25, 30, 34, 35). Specifically, the formation of β-PdH was observed during CO_2R, leading to the product selectivity change from formate to mainly hydrogen and CO (34, 36, 37). In addition, CO as a by-product poisons the Pd-sites and compromise the formate production (38). Various strategies such as bimetallic or non-metal elements doped Pd-based catalysts have been explored to weaken the intrinsic CO binding affinity on Pd surface, aiming to circumvent the fast decay of formate production at near-equilibrium potential (29, 36, 39–41). Besides, extrinsic strategies, e.g., pulsed electrochemical protocol to remove the surface CO, have been developed to extend the stability of formate production on Pd (42). While tremendous progress has been made, Pd-based catalysts still suffer from fast deactivation during CO_2R. Thus, it remains desirable to tackle on the above challenges and retain the high activity of Pd over a broad potential window to achieve energy efficient and practical relevant formate production from CO_2R (43).

In this work, we report an unexpected but profound stabilizing effect from the capping ligand polyvinylpyrrolidone (PVP, structure shown in *SI Appendix*, Fig. S1) introduced onto the Pd surface. Specifically, we found that it is not straightforward to completely remove the capping ligand after the Pd nanoparticle preparation, however, instead of

Significance

Electrochemical reduction of CO_2 offers great opportunity to turn waste carbon into value-added chemicals/fuels and further mitigate the pressing carbon emission issues. In particular, CO_2 reduction to formate has drawn tremendous attentions due to its promising near-term economic feasibility. One major hurdle for the practical implementation of this process is the unsatisfactory energy efficiency, as the energy input for activating the inert CO_2 molecule is significant. Pd-based electrocatalysts can activate CO_2 with minimal energy requirement; however, they suffer from rapid deactivation during CO_2 electroreduction. We report an effective strategy to prevent the deactivation of Pd-catalysts, that is, using a capping ligand to stabilize the high-valence Pd-species and further suppress the undesired Pd phase transition, which is the origin of Pd-catalyst deactivation.

Author contributions: L.W. designed research; Y.Z., X.L., Jingyi Chen, Junmei Chen, Jiayi Chen, L.F., H.Y., L.S., and L.W. performed research; S.X. and L.W. contributed new reagents/analytic tools; Y.Z., X.L., Jingyi Chen, Junmei Chen, Jiayi Chen, L.F., H.Y., S.X., L.S., and L.W. analyzed data; and Y.Z., X.L., Jingyi Chen, Junmei Chen, Jiayi Chen, L.F., H.Y., S.X., L.S., and L.W. wrote the paper.

The authors declare no competing interest.

This article is a PNAS Direct Submission.

[1]Y.Z., X.L., and Jingyi Chen contributed equally to this work.

[2]To whom correspondence may be addressed. Email: wanglei8@nus.edu.sg.

This article contains supporting information online at https://www.pnas.org/lookup/suppl/doi:10.1073/pnas.2218040120/-/DCSupplemental.

Published May 22, 2023.

suppressing the CO_2R (i.e., active sites blocking), the surface residue PVP promotes and stabilizes the formate production on Pd. Through detailed physical and electrochemical characterization, kinetic analysis, and first-principle simulations, we conclude that the PVP tends to stabilize the $Pd^{\delta+}$ species resulting from the catalyst preparation and pretreatment, which can suppress the undesired Pd phase transition from α-PdH to β-PdH, and further the formation of CO and H_2 (35, 38). Based on these insights, we purposely introduced PVP coatings onto the Pd surface and then tested them for CO_2R. As expected, both enhanced activity (typically by more than an order of magnitude under the same overpotentials) and much extended potential window (from −0.1 to −0.7 V vs. RHE) for formate production have been achieved. Taken together, our study discovers a new strategy for designing active and selective Pd-based electrocatalysts for formate production.

Results and Discussions

Promotion Effects of PVP on the Formate Production on Pd. In this work, we synthesized Pd nanocubes with similar sizes (*SI Appendix*, Fig. S2) as the model catalyst to avoid, at least to the best extent, complications resulting from particle size, facet, roughness factor, etc., which were demonstrated to have different effects on CO_2R (44). Per our observations, the as-synthesized Pd nanocubes (denoted as Pd) exhibited common activity and deactivation trends for formate production, similar to what was observed previously (45). Specifically, the corresponding CO_2R selectivity shifted to CO along with the increase of overpotential (Fig. 1*A*), and no detectable formate was produced by Pd in our experiment (*SI Appendix*, Fig. S3) at −0.5 V vs. RHE. Separately, we found there were residual PVP ligand on the Pd surface via X-ray photoelectron spectroscopy (XPS, *SI Appendix*, Fig. S4), despite that the Pd nanocubes were thoroughly washed by different solvents. Thus, we further employed sodium borohydride ($NaBH_4$) to remove the residual PVP based on a previous procedure (46, 47). Physical characterizations were conducted for the $NaBH_4$-treated Pd nanocubes (denoted as NT-Pd), the results show that the PVP was successfully removed, and no compositional changes occurred after this treatment (*SI Appendix*, Fig. S2). However, when tested for CO_2R under the same conditions, the NT-Pd exhibited an obviously decreased activity towards formate production and a reduced potential window compared to the as-synthesized Pd (Fig. 1*B*). Based on this observation, we tentatively believe that the PVP ligand is likely to have a promotion effect on CO_2R, instead of blocking the active sites. In addition to the borohydride treatment, we also applied positive cyclic voltammetry as electro-treatment (ET) aiming to clean the as-synthesized Pd surface (*SI Appendix*, Fig. S5). Surprisingly, the electro-treated Pd nanocubes (ET-Pd) showed an improved activity and slightly extended potential windows for the formate production (Fig. 1*C*). Besides, the XPS result suggests that the PVP retained after the electrotreatment. The combined results further confirmed our hypothesis of that the PVP ligand does have a promotion effect on CO_2 to formate conversion on Pd, and the electrotreatment can amplify this promotion effect.

To explore the PVP effect systematically, we purposely introduced PVP ligand to the as-synthesized Pd nanocubes (see details in the experimental section) and performed electro-treatment to the obtained samples. Note, the PVP loading within these samples is also estimated based on the ICP-MS results indirectly (*SI Appendix*, Table S1). As shown in Fig. 1 *D*–*F*, we found that ET-PVP-Pd with treated with modest PVP concentration (0.02 M) shows the best performance for formate production across a broad potential window. Excessive PVP loading will lead to activity loss, which most likely is due to the active-sites blocking effect (*SI Appendix*, Figs. S6 and S7). Moreover, the morphological structure of Pd nanocubes retained after both the electrotreatment and the CO_2R measurement (*SI Appendix*, Fig. S8). In the following, we focus on the sample of ET-PVP-Pd and study the PVP effect. The first appealing phenomenon we observed was that the potential window of formate production was extended to −0.7 V vs. RHE on ET-PVP-Pd, together with enhanced selectivity and activity. Under nearly all electrode potentials, ET-PVP-Pd achieved improved activity for formate production compared with the model catalysts Pd and NT-Pd, by at least one order of magnitude (Fig. 1*G*). For instance, the partial current density of formate on ET-PVP-Pd reached −6.5 mA cm^{-2} at −0.3 V vs. RHE (Fig. 1*F*), which was ~10 times and ~20 times of those on as-synthesized Pd catalyst (Fig. 1*A*) and NT-Pd (Fig. 1*B*), respectively, at −0.3 V vs. RHE (Fig. 1*G*). We observed similar performance trends after normalizing the formate production activities to the corresponding catalyst mass loadings and electrochemical active surface area (*SI Appendix*, Figs. S9–S11), indicating that the intrinsic activity of Pd has been improved after the PVP coating. Moreover, we conducted CO_2R experiments based on PVP-treated Pd catalyst in a vapor-fed reactor and observed significantly improved performance for formate production (*SI Appendix*, Figs. S12 and S13). Even though the deactivation of Pd still occurs at high overpotentials, we believe the combination of efficient Pd catalyst (high activity at low overpotentials) and anti-deactivation strategies [i.e., PVP effect, alloying (40, 50, 51)] will provide us opportunities in achieving highly energy efficient formate production. Thus, it remains desirable to continuously develop new Pd-based catalysts with enhanced intrinsic activity. Note, unlike Pd and NT-Pd (Fig. 1 *A* and *B* and *SI Appendix*, Fig. S14) (52), on which the CO_2R current decreased and reached a plateau quickly, the CO_2R current on ET-PVP-Pd was much more stable, however, still suffering deactivation especially under more negative potentials (*SI Appendix*, Fig. S15 and Note S1). This deactivation led to difficulties in analyzing both gas-phase and liquid-phase products at a precise and short time period, we thus only sought to report the averaged activity and selectivity for formate production on these catalysts (*SI Appendix*, Fig. S15 and Tables S2–S5). Nonetheless, we conclude that PVP coating can lead to improved activity and selectivity toward formate production on Pd surface over an extended potential window, and the CV-treated PVP-Pd catalysts (i.e., ET-PVP-Pd) exhibit superior performance (*SI Appendix*, Fig. S16) comparable to, if not outperform the documented Pd-based materials prepared by advanced synthetic strategies (Fig. 1*H*). Note, this PVP promotion effect is applicable to Pd-catalysts with different facets and morphologies (e.g., Pd nanoparticles and Pd nanowires, *SI Appendix*, Figs. S17 and S18), suggesting that PVP coating can be a versatile approach for promoting formate production on Pd surface.

Exploring the PVP Effect via Structural and Electronic-State Characterizations. Our model catalyst, Pd nanocubes (Pd), was prepared based on a solution method using PVP as a stabilizing agent (53). As shown in Fig. 2 *A* and *C* [the transmission electron microscopy (TEM) image], Pd nanocubes exhibit highly monodispersed cubic morphology with an average size of 10 ± 2 nm. High-resolution TEM (HRTEM) images and the corresponding inverse fast Fourier transform (FFT) were collected and analyzed (Fig. 2*A*), confirming the desired crystallinity nature and clear lattice fringes of Pd cubes. The X-ray crystallography (XRD) patterns (Fig. 2*J* and *SI Appendix*, Fig. S19) also suggest a good crystallinity of these Pd-based

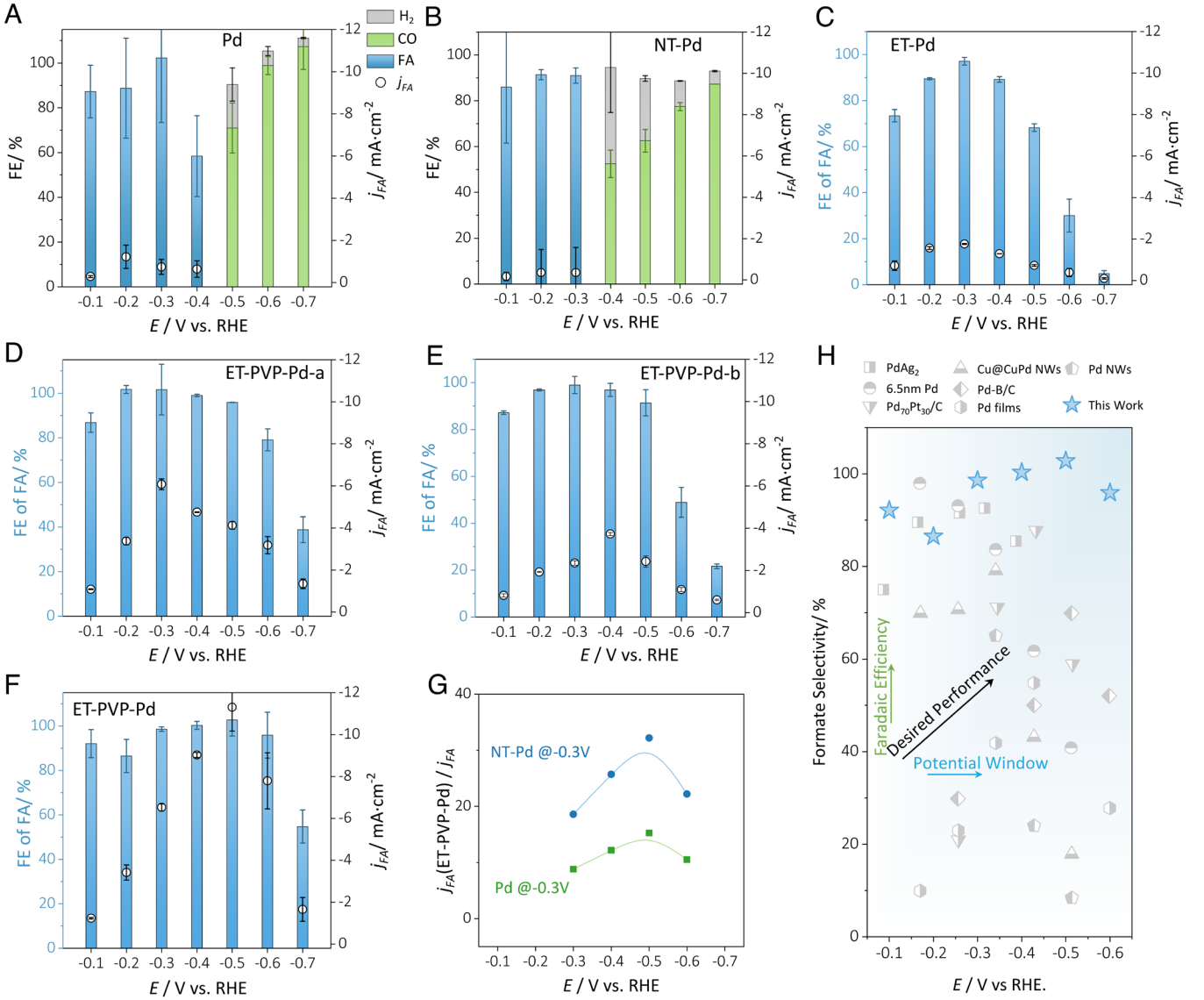

Fig. 1. CO_2 electroreduction performance. FE values (*Left*) and partial current densities (*Right*) for formate production on (*A*) Pd, only liquid-phase is labeled from −0.1 V to −0.4 V vs. RHE and all products are labeled from −0.5 V to −0.7 V vs. RHE; (*B*) NT-Pd, only liquid-phase is labeled from −0.1 V to −0.3 V vs. RHE and all products are labeled from −0.4 V to −0.7 V vs. RHE; (*C*) ET-Pd; (*D*) ET-PVP-Pd (NT-Pd treated in 0.02 M PVP solution, followed by CV treatment); (*E*) ET-PVP-Pd-a (NT-Pd treated in 0.01 M PVP solution, followed by CV treatment); and (*F*) ET-PVP-Pd-b (NT-Pd treated in 0.05 M PVP solution, followed by CV treatment), at different applied electro-potentials in CO_2 saturated 0.1 M $KHCO_3$. (*G*) Formate production enhancement factor (ratio of partial current densities) of ET-PVP-Pd electrode over potential window of −0.3 V to −0.6 V vs. RHE compared with NT-Pd at −0.3 V and Pd at −0.4 V vs. RHE. (*H*) Comparison of this work with the state-of-the-art Pd-based electrocatalysts for CO_2R to formate. [$PdAg_2$ (40), Cu@CuPd NWs (36), Pd NWs (31), 6.5nm Pd (48), Pd-B/C (26, 49), $Pd_{70}Pt_{30}$/C (28), Pd films (49)]. Note, the FE of gas-phase products are not plotted unless they can be measured and analyzed accurately (*SI Appendix*, Note S1).

catalysts with ordered long-range structure, corresponding well with the above microscopic results. As discussed above, the sodium borohydride-treated Pd (NT-Pd) and the PVP-coated Pd (PVP-Pd, Fig. 2 *D* and *E–H* and *SI Appendix*, Fig. S20) were prepared from the as-synthesized Pd nanocubes (54). Clearly, the presence of the PVP can suppress the Pd-particles aggregation (Fig. 2*B* and *SI Appendix*, Fig. S2), while it may not help improve the intrinsic activity of the Pd, it is a bonus for achieving improved mass activity. The EDX (energy-dispersive X-ray spectroscopy) elemental mapping and TEM images both indicate the uniform PVP distribution across the surface of Pd crystals (Fig. 2 *D* and *E–H*). Besides, Raman spectroscopy was employed to further confirm the existence of PVP (Fig. 2*I*). The Raman peaks associated with the surface PVP appear at ~1,580 cm^{-1}, blue-shifted compare to the pure PVP sample [the C=O stretch peaks locate at 1,700 to 1,630 cm^{-1} (55)]. This noticeable Raman peak shifting is likely resulted from the specific vibrational modes of PVP moieties that interacted with Pd (54). In the contrary, no detectable Raman signals were observed for NT-Pd and Pd due to none or trace amount of PVP existed on the Pd surface (Fig. 2*I*). Moreover, we further confirmed the existence of PVP in the as-synthesized Pd samples as well as the removal of PVP in NT-Pd (*SI Appendix*, Fig. S4) by analyzing the N *1s* signals in XPS. Overall, structural characterizations illustrate that the removement of residual PVP on the Pd model catalyst and the preparation of PVP-Pd assembles were both successful, facilitating the study of the above PVP effect.

The electronic structure of all the Pd-catalysts, particularly the Pd-PVP derived samples, were investigated by XPS and X-ray absorption spectroscopy (XAS). The high-resolution XPS Pd 3d signals for all samples showed a doublet at binding energies of 335.5 eV and 341 eV, which can be assigned to Pd $3d_{5/2}$ and Pd $3d_{3/2}$, respectively (Fig. 2*K*). Through careful curve fittings, we can deconvolute these Pd 3d signals into two pairs of peaks, corresponding to the species of Pd (0) and Pd^{2+} at 335.5/340.8 eV and

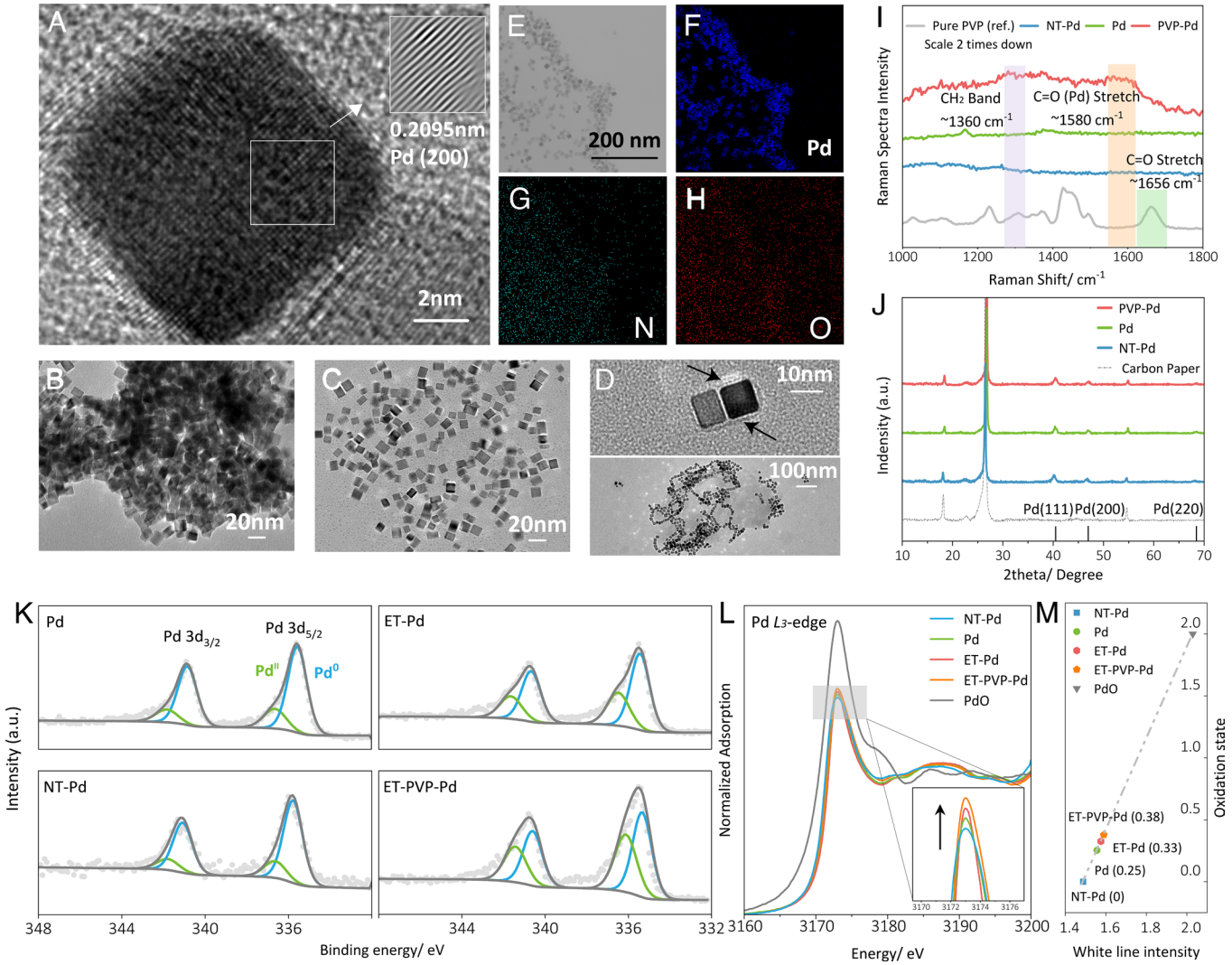

Fig. 2. Structural and electronic state characterizations. (*A*) High-resolution TEM image of the as synthesized Pd nanocubes (*Inset* is the inverse-FFT pattern of the corresponding area). (*B–D*) TEM images of NT-Pd, Pd, and PVP-Pd. (*E–H*) TEM-EDS mapping images of PVP-Pd. (*I*) Raman spectra of Pd, ET-Pd, NT-Pd, and ET-PVP-Pd. (*J*) XRD pattern of PVP-Pd, Pd, and NT-Pd electrodes. (*K*) High-resolution Pd 3d XPS spectra of Pd, ET-Pd, NT-Pd, and ET-PVP-Pd electrodes. (*L*) Normalized XANES at Pd L_3-edge of Pd, ET-Pd, NT-Pd, ET-PVP-Pd, and PdO. (*M*) The average oxidation states fitted *via* XANES spectra in *L*.

336.6/341.8 eV, respectively (56). The Pd^{2+} species were likely resulted from the formation of native oxide layer on the ultra-small Pd nanoparticles when exposing the air. Here, we tentatively assigned these high-valence-state Pd as the $Pd^{\delta+}$ species (Fig. 2*K*), which are likely the convolution of multiple oxidative Pd species with different chemical environments. Notably, the presence of PVP and the electrotreatment seems to promote the formation of $Pd^{\delta+}$ species, based on the increased sizes of the $Pd^{\delta+}$ peak (Fig. 2*K*). Thus, we suppose that the oxidative species are generated during the synthetic procedure (when exposed to air) as well as the electro-treatment (oxidative CVs), and the presence of the PVP can stabilize these high-valence-state Pd species. To confirm this, X-ray absorption near-edge spectroscopy (XANES) was conducted for the Pd L3-edge of these samples to further study their hierarchical electronic states. As shown in Fig. 2 *L* and *M*, we can estimate the average valence states of the Pd catalysts by analyzing the white-line intensity using NT-Pd electrode (0) and PdO (2+) as the references. These results correspond well with the above XPS results, more $Pd^{\delta+}$ species were observed in the sample of ET-PVP-Pd. Note, different from XPS, XAS is bulk measurement which takes into account all the Pd atoms within a given sample, thus, the noticeable difference on the average valence state suggests that there are significant differences among these Pd surfaces. Overall, we found that there are $Pd^{\delta+}$ species exhibited on the Pd surface after the preparation and electrotreatment, and the presence of PVP can stabilize these high-valence Pd species. We believe that the improved performance of the PVP-treated Pd toward formate production is closely associated with the presence of the $Pd^{\delta+}$ species, since it is the most profound difference between the PVP-Pd and pristine Pd based on the above physical characterizations.

Theoretical Origin of the Efficient Formate Production on $Pd^{\delta+}$-Riched Surface. As aforementioned, the high-valence $Pd^{\delta+}$ species are largely generated through the electrotreatment (CV cycles) (Fig. 2*K*), and the CVs were conducted to a potential range that Pd to Pd-OH occurs (57). Thus, we tried to introduce the *OH species to the Pd surface to model the $Pd^{\delta+}$ species and explore its effect on CO_2R theoretically. First, the *OH affinity on pristine Pd (200) and PVP-Pd (200) surface was investigated by computing the corresponding adsorption energies (Fig. 3*A*). In agreement with our experimental observations, PVP stabilizes the *OH adsorbates by as much as 1.15 eV compared with the pristine Pd (200) surface, indicating that PVP-Pd (200) could improve

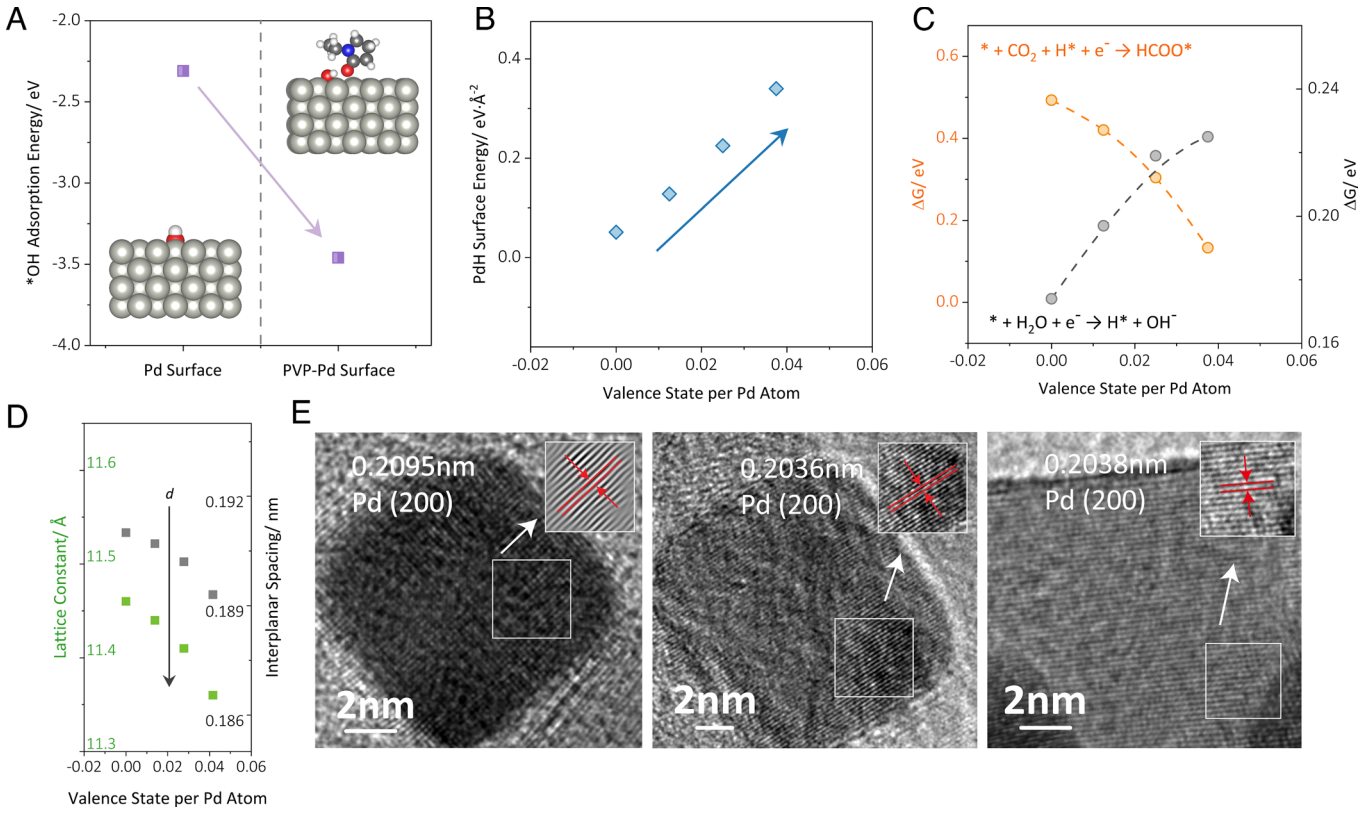

Fig. 3. Theoretical investigations. (*A*) *OH adsorption energies on Pd (200) and PVP-Pd (200) surface (inset is the geometry structure of *OH adsorption). (*B*) PdH (200) surface energy with different valence states. (*C*) HCOO* adsorption-step energy barrier for CO_2R and Volmer-step energy barrier for HER on Pd (200) surface with different valence states. (*D*) The theoretically computed lattice constant of Pd (331) (*Left*) and interplanar spacing (*Right*) of PdH slab on the function of the valence states. (*E*) High-resolution TEM images of the as-synthesized Pd-nanocube, ET-PVP-Pd, and post-catalysis ET-PVP-Pd (from left to right) (*Inset* is the inverse-FFT pattern of the corresponding area, post-catalysis TEM is conducted after reduction under −0.7 V vs. RHE for 30 min).

the *OH affinity and its coverage under relevant conditions. This result agrees well with our hypothesis that the $Pd^{\delta+}$ species are likely resulted from the *OH adsorption, especially after the CV treatments. Consequently, we calculated the PdH surface energy with different hierarchical valence states to probe the stability of the above Pd surfaces under the catalytic conditions. As shown in Fig. 3*B*, the surface energy of PdH increases linearly from 0.05 to 0.34 eV/Å^2 along with the increase of the valence state (from 0 to 0.04 e$^-$/per atom), suggesting that higher valence state is unfavorable for the formation of PdH surface and further inhibit the PdH phase transition. Then, thermodynamic barriers for CO_2R and hydrogen evolution reaction (HER) on Pd surfaces with different oxidation degree, are obtained from calculations based on density functional theory (DFT), specifically presented by Gibbs free energy diagram based on the computational hydrogen electrode model (58) (*SI Appendix*, Table S8). Typically, in neutral condition (0.1 M $KHCO_3$), formate production and HER proceed simultaneously on Pd (200) surface while the CO_2 adsorption (HCOO*) step and Volmer step (*H) are assumed to be the rate-limiting steps (RDS) for these two reactions, respectively (33, 59, 60) (*SI Appendix*, Fig. S21). As expected, we observed that the energy barriers of the CO_2 adsorption for formate decreases (from 0.493 to 0.133 eV, Fig. 3*C*) along with the increase of the Pd-surface valence state, in agreement with our experimental observations. In contrast, higher valence state inhibits the Volmer step of HER, implying that $Pd^{\delta+}$ species tend to suppress the HER activity. To further evaluate the versatility of the PVP effect, corresponding theoretical investigations are conducted the for Pd (111) surface. As expected, the same activity and selectivity trends are observed (*SI Appendix*, Fig. S22), in line with the above experimental results (*SI Appendix*, Figs. S17 and S18). In addition, we modeled the effect of the Pd-slab valence state on the lattice constant and interplanar spacing. As the valence state of the Pd increases, one should expect a decrease in the lattice constant (interplanar spacing, Fig. 3*D*), which is in line with what we observed via high-resolution TEM images (Fig. 3*E*). Note, this decreased lattice constant of ET-PVP-Pd retained after CO_2R under −0.7V vs. RHE (Fig. 3*E*), suggesting that the PVP ligand may be able to stabilize the $Pd^{\delta+}$ species even under the catalytic conditions. Well-controlled *operando* measurements are crucial to further confirm this assumption. Nonetheless, with the decreased lattice distance, H-atoms intercalations into the Pd lattice become more difficult. To conclude, with these theoretical investigations, we further confirm our hypothesis: PVP-stabilized $Pd^{\delta+}$ is the origin of the improved activity and selectivity for the formation production.

Electrochemical Characterizations for ET-PVP-Pd to Inhibit Pd Phase Transition and CO Poisoning. To further probe the PVP effects, we investigated the adsorbed chemical species on Pd after CO_2R electrolysis via CVs (Fig. 4 *A* and *B*). Specifically, as shown in Fig. 4*A*, we first recorded the coulometric curves for the different Pd-catalysts (at −0.7 V vs. RHE) to pass the same amount of charges. Subsequently, CVs at positive potential range were performed and analyzed after each electrolysis. As shown in Fig. 4*B*, the first anodic scan of the CVs present peaks associated with the CO stripping (CO_{strip}) of the Pd surfaces, which are closely associated with the Pd phase transition and CO poisoning. Specifically, the anodic peaks located at 0.53 and 0.69 V vs. RHE correspond to the stripping of the adsorbed

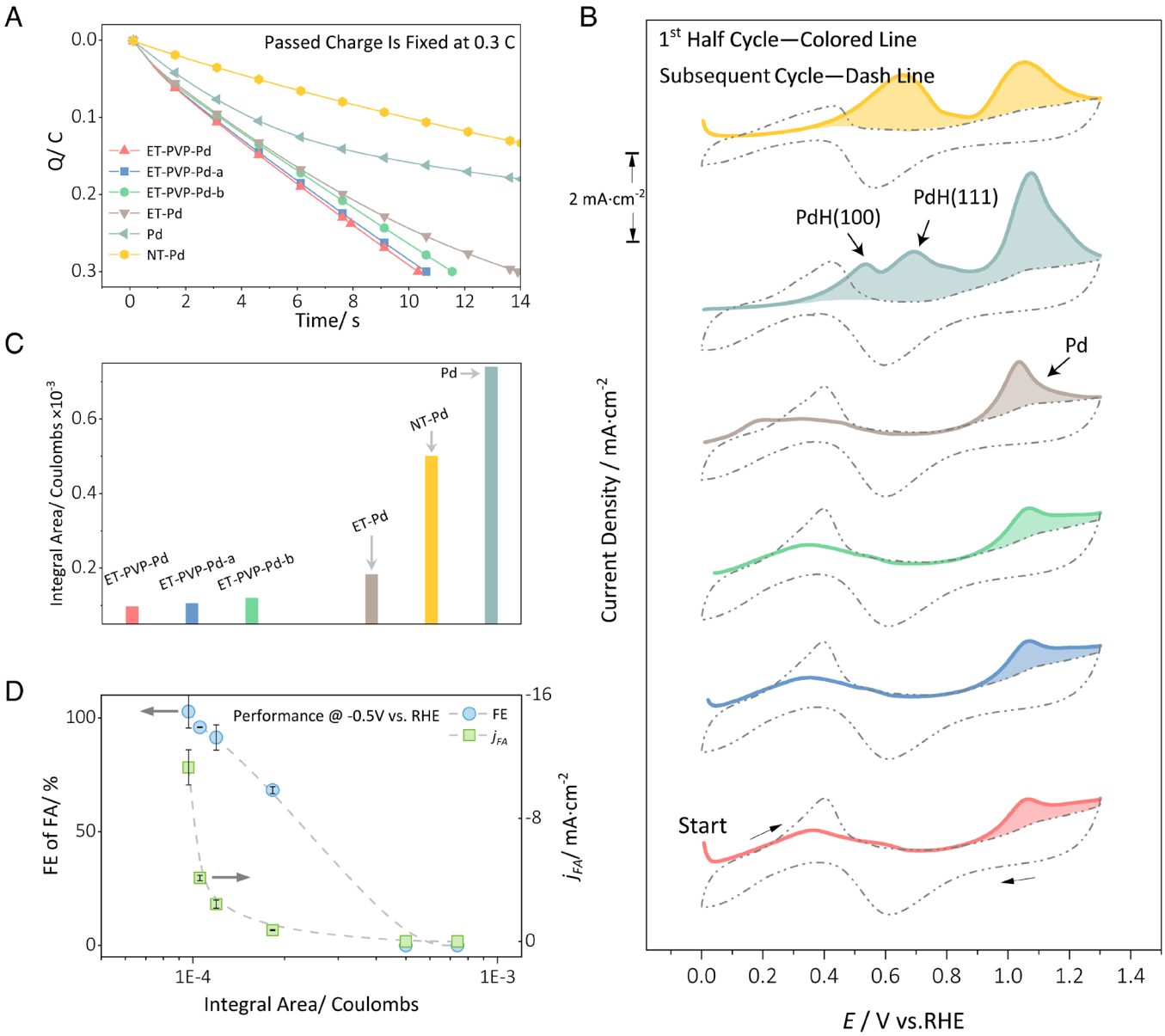

Fig. 4. Electrochemical characterizations of the surface adsorbed species. (*A*) Coulometric curves vs. time of the catalyst candidates at −0.7 V vs. RHE in a CO_2-saturated 0.1 M $KHCO_3$ electrolyte. In a typical electrolysis, passed charge is fixed at 0.3 C. ET-PVP-Pd, ET-PVP-Pd-a, and ET-PVP-Pd-b indicate different concentrations of PVP in synthesis (0.02 M, 0.01 M, and 0.05 M, respectively). (*B*) CO stripping voltammogram for catalyst candidates after the electrolysis. Scan rate: 10 mV s^{-1}. In the first half cycle, the anodic peaks related to CO stripping (CO_{strip}) of different Pd-catalysts are indicated with different colors. (*C*) Integral areas of the CO stripping peaks in *B*. (*D*) Relation between CO poisoning area and electrochemical performance of the corresponding Pd-catalyst. Same color labels are used for *A*, *C*, and *D*.

CO on PdH (100) and PdH (111), whereas the stripping peaks associated with stronger bonded CO (i.e., adsorbed CO on pure Pd sites) located at 1.05 V vs. RHE (32). Both the as-synthesized Pd and NT-Pd samples exhibited large CO striping peaks at PdH regimes as well as pure Pd regime, indicating severe Pd to PdH phase transition and the consequent CO poisoning occurred to both samples. Only one large CO striping peaks was observed for the NT-Pd at the PdH regimes, this peak convolution is likely due to particle aggregation and morphological reorganization (46), in line with the above TEM image (Fig. 2*B*). In the contrary, only one single CO_{strip} peak was observed for ET-Pd and other electrotreated PVP-Pd samples. This is a clear indication that PdH (or β-Hydride (34, 35)) formation can be impeded in presence of the high-valence Pd species under the catalytic conditions. In addition, the smaller sizes of the CO stripping peaks of the PVP-Pd samples (Fig. 4*C*) compared to the as-synthesized Pd (with some residue PVP on the Pd surface) further confirms the positive effects of PVP. Besides, the previous activity trend observed for samples with different PVP loadings was also appeared in these experiments (Fig. 4 *A* and *B* and *SI Appendix*, Fig. S23), confirming that only certain amount of PVP is needed to stabilize the surface $Pd^{\delta+}$, excess PVP loading will block the active-sites and imped CO_2R. As suggested previously, the CO_{strip} peaks tend to compete with the H extraction (H_{ext}, H atoms extracting from Pd lattice), H desorption (H_{des}, H atoms desorbing from the Pd surface) peaks as the electrolysis potential decrease (42), thus no characteristic H-related peaks were observed in our experiments (*SI Appendix*, Note S2). Taken together, the above surface analysis matched well with the CO_2R performance on the corresponding Pd catalysts (Fig. 4*D* and *SI Appendix*, Note S3), we thus conclude that the electrochemical Pd phase transition and CO poisoning were significantly inhibited by the presence of $Pd^{\delta+}$ species which are stabilized by the PVP ligand.

Kinetic Investigations via Electrochemical Impedance Analysis. Next, we turn our attention to investigating the role of $Pd^{\delta+}$ species on the interfacial charge transfer kinetics. Electrochemical impedance spectroscopy (EIS) was employed under the catalytically relevant conditions (−0.3 V vs. RHE). For a typical two-electron process, assuming the adsorption step occur without diffusion limitation (61), the first semicircle at high frequencies is associated with the charge transfer resistance (R_{ct}) and the double-layer capacitance (C_{dl}), and the second semicircle at lower frequencies represents the pseudocapacitive behavior related to adsorption resistance (R_p) and pseudocapacitance (C_p) (Fig. 5 *A* and *B* and *SI Appendix*, Note S4). We thus focus on analyzing these three resistance components (R_s, R_p, and R_{ct}) in the equivalent circuit to reveal the detailed electrode kinetics. The EIS fitted results indicate that the ET-PVP-Pd and ET-Pd showed significantly smaller R_p (8.8 ohm and 8.7 ohm, respectively) in comparison with that of Pd electrode (19.7 ohm, Fig. 5*G* and *SI Appendix*, Table S6), indicating a substantially accelerated CO_2 adsorption process (First step in Fig. 5*B*). This is in a good agreement the above DFT calculations, the CO_2 activation and adsorption on the Pd surface can be greatly promoted in the presence of surface Pd^+ species. With regard to NT-Pd, as expected, our EIS results indicated that the CO_2R kinetics is limited by CO_2 adsorption (Fig. 5*G* and *SI Appendix*, Note S5). Overall, the EIS results once again confirm the significance of PVP-stabilized $Pd^{\delta+}$ species for achieving facile electrode kinetics for CO_2R.

Tackling the Stability Issue for Pd-Based Catalysts. The key challenge for Pd-based catalysts is to prevent the catalyst degradation causing by PdH phase transition and CO poisoning. While ET-PVP-Pd presented improved CO_2R activity and selectivity, its stability is still unsatisfactory especially at more negative potentials. Thus, several instructive strategies were employed in our catalytic system to prevent catalyst degradation caused by CO poisoning. First, we introduced small portions of O_2 into the CO_2 stream during CO_2R inspired by previous work (62, 63). As shown in Fig. 6*A*, the presence of O_2 promoted the formate production rate significantly at fairly negative potential (−0.7 V vs. RHE). This is likely due to the interaction between surface oxygen and CO species, which further facilitate the removal of CO from Pd surface. However, this improved activity is achieved on the expense of largely decreased current efficiency towards the desired CO_2R (*SI Appendix*, Fig. S24), as the thermodynamically favored competing reaction, oxygen reduction reaction occurred rapidly during the co-feeding experiment. Thus, we further explored a cyclic electrolysis through applying alternative potentials during the CO_2R (Fig. 6*B*) based on a modified procedure reported elsewhere (42). A typical cycle of the electrolysis consists of one reduction step and one oxidation LSV as shown in Fig. 6*B*. Specifically, −0.4 V vs. RHE was applied to the electrode for 5 min, followed by a linear sweep voltammetry (LSV) from 0 to 1.4 V vs. RHE with the scan rate of 20 mV/s. During the anodic LSV, the stripping of adsorbed CO and hydrogen occurred predominantly (*Right Inset* in Fig. 6*B* and *SI Appendix*, Note S6), providing fresh active sites for formate formation on the ET-PVP-Pd. As a result, ET-PVP-Pd afforded a high formate FE of 96.7 % and partial current density of −10.89 mA cm^{-2} for an over 10-h electrolysis. In contrast, stability test of the ET-Pd catalyst using the same cyclic electrolysis was conducted to make a direct comparison with the PVP-treated sample (*Left Inset* in Fig. 6*B*). As expected, both the activity and selectivity for formate production were promoted significantly upon the addition of the PVP coating during the entire stability testing period. In addition, we also conducted a temperature-dependent CO_2R experiments. We found that the activity and selectivity of formate first increased with the increase of temperature, then both dropped due to the quickly raised HER competing reaction. Using the above strategies in understanding the surface species, we found that the peak positions for CO stripping shifted to less positive potentials and the corresponding peak areas descended in sequence (*SI Appendix*, Note S7 and Figs. S25 and S26) along with the increase in temperature, suggesting that higher temperature can accelerate the CO desorption and slow down the catalyst degradation. Note, we do not exclude the influence of CO_2 solubility changes due to the temperature increase, which may also lead to the rise of HER. Overall, while these strategies addressed the stability issue for Pd-based catalysts to some extent, new strategies are still desired particularly those can improve the intrinsic stability of Pd-based materials for CO_2R.

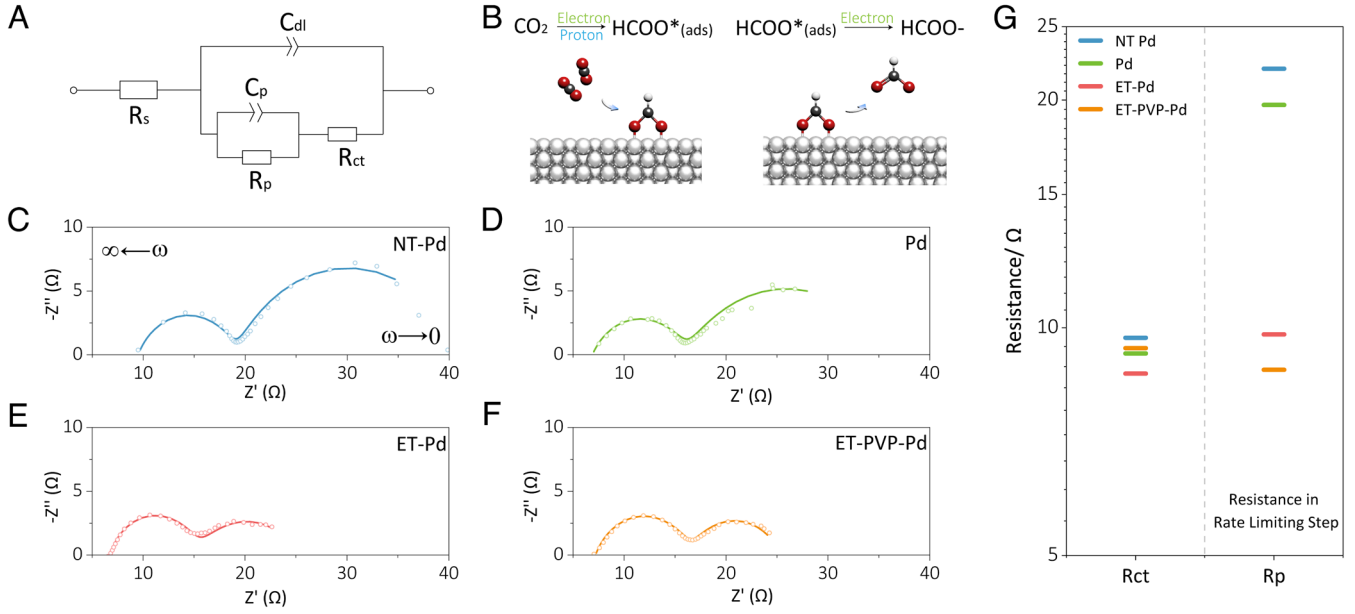

Fig. 5. Electrochemical impedance spectroscopy. (*A*) The equivalent circuit used for the curve fitting. C_{dl} and C_p are the constant phase elements, representing double-layer capacitance and pseudo capacitance, respectively. R_s is the solution resistance; R_p is the adsorption resistance; R_{ct} is the charge transfer resistance. (*B*) Illustration of two steps pathway for the formate formation from CO_2. (*C–F*) Fitted Nyquist plots of the electrochemical impedance spectra of NT-Pd, Pd, ET-Pd, and ET-PVP-Pd at −0.3 V vs. RHE in CO_2 saturated 0.1 M $KHCO_3$. Solid line is the simulated curve. ω is the frequency. (*G*) The fitting values for each of the resistance components.

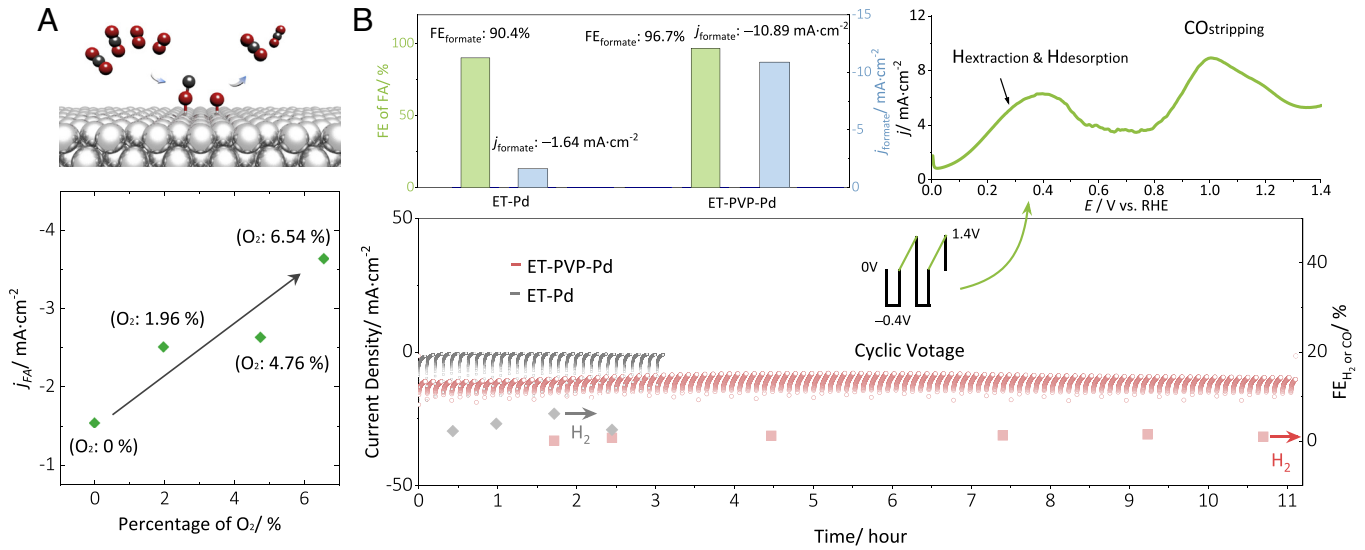

Fig. 6. Strategies for improving the stability. (*A*) CO_2R in presence of small portions of O_2. *Left*: formate partial current density on ET-PVP-Pd electrode at −0.7 V vs. RHE in 0.1 M $KHCO_3$ vs. O_2 concentration. *Top*: schematic illustration of *CO removal from the Pd surface by the surface *O species (O atoms are red and C atoms are black). (*B*) CO_2R on ET-PVP-Pd and ET-Pd by the cyclic electrolysis. The red and pink data represent the total current density of CO_2R and the H_2 selectivity on the function of time, respectively. The grey line: current density, grey points: H_2 selectivity (ET-Pd catalyst in cyclic electrolysis). The *Left Inset* summarizes the FA production of ET-Pd and ET-PVP-Pd electrodes in cyclic electrolysis, respectively. The *Inset* LSV shows anodic peaks associated with H_{ext}, H_{des}, and CO_{strip}.

Conclusions

In summary, we observed a promotion effect of PVP on Pd-based CO_2R to formate, and revealed the origin of this promotion effect, that is the PVP-stabilized $Pd^{\delta+}$ species can promote the formate pathway and inhibit the undesirable PdH formation, and further suppress the competing H_2 and CO formation. As a result, both broad potential window (up to −0.7 V vs. RHE) and enhanced intrinsic activity (more than an order of magnitude compared to the pristine Pd-surface) towards formate production can be achieved on the PVP-Pd catalysts. Besides, we found that this phenomenon is applicable to other Pd-catalysts (e.g., Pd nanoparticles and Pd nanowires). Based on these PVP-Pd catalysts, we proposed and evaluated system-level strategies aiming to address the stability issue for Pd-based catalyst and achieved efficient formate production. Future studies focusing on revealing the valence state of Pd during CO_2R via the state-of-the-art *operando* measurement will add more insights to this system. Overall, we believe that the design strategy of surface engineering established in study can be applied broadly to other energy applications that depend on high performance of electrocatalysis.

Experimental Methods

Catalysts Synthesis and Electrode Preparation. Pd nanocubes (Pd NCs) were prepared based on a modified literature method (64). Typically, 8.0 mL of an aqueous solution (18.2MΩcm resistivity, Milli-Q Direct Water Purification System) containing KBr (300 mg, ACS reagent, ≥99.0%, Sigma Aldrich), PVP (105 mg, average Mw ~ 55000, Sigma Aldrich), and L-ascorbic acid (60 mg, 99%, Sigma Aldrich) was added into a vial. The vial was heated in air under magnetic stirring at 80 °C in oil bath for 10 min. Subsequently, 3.0 mL of an aqueous solution of Na_2PdCl_4 (57 mg, 98%, Sigma Aldrich) was added with a pipette. After the vial had been loosely capped, the reaction could proceed at 80 °C in an oil bath for 3 h. The products were collected by centrifuging in water for three times (10,000 rpm, 10 min). Precipitates were redispersed in 11 mL water.

Preparation of NT-Pd. The removal of surfactant PVP from the surface of untreated Pd NCs was carried out using a $NaBH_4$ (powder, ≥98.0%, Sigma Aldrich) aqueous solution. In a typical process, 6 mg as-prepared Pd NCs were treated in 25 mL $NaBH_4$ aqueous solution ($NaBH_4$:H_2O = 1.9 mg:5 mL) with stirring for 30 min at room temperature. The treated Pd NCs sample was collected by centrifugation at 10,000 rpm for 10 min.

Preparation of PVP-Pd. After Pd NCs preparation, different amounts of PVP were added to 6.25 mL of deionized (DI) water to prepare aqueous suspensions containing 0.02 M, 0.01 M, 0.05 M, and 0.1 M of PVP. Subsequently, 6 mg of prepared Pd NCs was added to the PVP suspensions, mixing at room temperature for 12 h. Subsequently, the catalyst was collected by centrifugation at 10,000 rpm for 10 min. The synthesized catalysts were named as PVP-Pd, PVP-Pd-a, PVP-Pd-b, and PVP-Pd-c, according to the concentration of the PVP suspension (0.02, 0.01, 0.05, and 0.1 M respectively).

Electrotreatment (ET) of the Electrodes. The applied CV techniques scanned in the potential range from 0 to 1.3 V vs. RHE at a rate of 10 mV s−1 in CO_2-saturated 0.1 M $KHCO_3$ solution for 2 cycles. With the electrotreatment (ET), above electrodes were named as ET-PVP-Pd, ET-PVP-Pd-a, ET-PVP-Pd-b, and ET-PVP-Pd-c, according to the concentration of the PVP suspension (0.02, 0.01, 0.05, and 0.1 M respectively).

Materials Characterization. TEM images were captured by a JEOL JEM-2010 TEM (working voltage: 200 kV). FESEM images were taken on a JEOL, JSM-7610F field scanning electron microscopy. The X-ray diffraction (XRD) analysis was carried out by a Shimadzu XRD-6000 X-ray diffractometer with a Cu Kα irradiation source (λ = 1.54056 Å). The XPS analysis was done using a Thermo ESCALAB 250 (monochrome Al Kα, hν = 1486.6 eV). The Raman spectroscopy analysis was carried by using a Horiba Jobin Yvon Modular Raman Spectrometer with a laser wavelength of 633 nm. Pd L3-edge XANES data were collected at the XAFCA beamline of the Singapore Synchrotron Light Source under transmission mode. The energy calibration was made with a palladium oxide standard at 3,713 eV. The spectra were normalized using Athena software.

Product Analysis. Electrochemical CO_2R measurements were conducted in CO_2-saturated 0.1M $KHCO_3$ under ambient temperature to investigate the catalytic performance of Pd model catalyst (Pd nanocubes) and other samples using an H-type electrochemical cell comprising a catalyst-coated, carbon paper (AvCarb P75T) as the cathode, an Ag/AgCl electrode as the reference, a Pt foil as the anode and an anion exchange membrane (*SI Appendix*, Fig. S27). Electrolysis was conducted in H-cell with an AEM and a Nafion binder (Nafion 117) were used for anion and cation exchange, respectively. All potentials were controlled against an Ag/AgCl reference electrode using a Bio-Logic VMP3 multichannel potentiostat

and converted to the RHE reference scale (ERHE = EAg/AgCl + 0.197 V + 0.0591 pH). All potential values are given without iR correction.

Gas-phase products were identified and quantified by gas chromatography [GC, Shimadzu, GC-2014, equipped with a packed column, two flame ionization detectors (FID, for CO analysis) and one thermal conductivity detector (TCD, for H_2 analysis)]. A typically CO_2R experiment in this article is based on 30-min testing with a set potential (Fig. 1 and *SI Appendix*, Figs. S6, S17, and S18). During the test, the GC will perform three analyses on the gas-phase products, at the 5 min, 16 min, and 27 min, respectively. Since there is a 1-min pretreatment needed for a GC injection, the above gas-phase data are actually the gas-phase products located at 6 min, 17 min, and 28 min, respectively. The gas-phase products marked in the figures are the arithmetic mean of these three gas-phase data for the entire CO_2R test.

Liquid-phase products were identified and quantified by ^{1}HNMR spectroscopy. The concentration of produced $HCOO^-$ was estimated using a 400 MHz NMR spectrometer (Bruker). A typical ^{1}H NMR sample is prepared *via* mixing the post-treaction catholyte (700 μL, after 30 min CO_2R) containing the liquid product with the internal standard solution [D_2O (35 μL) containing 10 mM dimethyl sulfoxide (DMSO) and 50 mM phenol]. The partial current densities of gas products and formate are estimated from the GC data and NMR results, respectively. Then, the FE of the gas and liquid products are calculated by

$$FE = \frac{j_i}{j_{total}} \times 100\,\%$$

Total current densities for FE calculation are arithmetic mean of the current during the potentiostatic experiment.

Cyclic Electrolysis and Stripping Experiment. In cyclic electrolysis, the potential program includes one reduction step and one oxidation step per cycle. In the reduction step, −0.5 V vs. RHE was applied for 5 min, followed by linear sweep voltammetry from 0 to 1.4 V vs. RHE applied in the oxidation step with the sweep speed of 20 mV/s.

In CO stripping measurement, stripping measurement, we control the passed charge fixed at 0.3 C in the electrolysis at −0.7 V vs. RHE. RHE for the electrolysis. After electrolysis, anodic CV was scanned in the potential range from 0 to 1.3 V vs. RHE at a scan rate of 10 mV s1, in CO_2-saturated 0.1 M $KHCO_3$ for two cycles. To calculate the amount of COstrip charges, the area of oxidation peaks was integrated and the charge caused by double-layer charging and oxide formation was subtracted:

$$Q = \int_0^t I \times dt$$

where Q is oxidation charges, *I* is oxidation current, and *t* is time.

Computational Calculation Method. We performed first-principles calculations by the Vienna ab initio simulation package (VASP) with the projector augmented wave (PAW) formalism (33, 59). The exchange-correlation interaction was employed by the Perdew–Burke–Ernzerhof (PBE) functional with generalized gradient approximation (GGA) (60). We set a plane-wave cutoff of 500 eV for all the computations in this study. The 3 × 3 × 4 supercell of Pd (200) slab (total of 72 atoms) was built with a vacuum of 15 Å. The top three layers of the Pd (200) slab surfaces including adsorbates were relaxed in the calculations, while the bottom layer was fixed. We used 3 × 3 × 1 and 7 × 7 × 1 Monkhorst-Pack k-point grids for the geometric optimization and energy calculation, respectively. The convergence criteria of energy and forces acting on each atom were 10^5 eV and 0.02 eV Å^1, respectively, in the geometry optimization.

To calculate the Gibbs free energy diagram, the computational hydrogen electrode model was employed where each electrochemical reaction step is treated as a simultaneous transfer of the proton-electron pair as a function of the applied potential. Gibbs free energies for relevant species were calculated with the expression as (58):

$$G = E_{DFT} + E_{ZPE} - TS$$

where E_{DFT} is the calculated DFT electronic energy, E_{ZPE} and *TS* refer to zero-point energy and entropy contributions. The underlying reaction mechanism of the formation for HCOO* is as follows:

$$CO_2\,(g) + H^+\,(aq) + * + e^- \rightarrow HCOO*$$

where "*" is the active site. Using the initial state where gaseous CO_2 molecules are freely above an empty surface, the Gibbs free energy difference of interest can finally be expressed as:

$$\Delta G\left[HCOO*\right] = G\left[HCOO*\right] - \left(G\left[*\right] + G\left[CO_2\right] + G\left[H^+ + e^-\right]\right)$$

The Volmer step of the HER in alkaline media is described as (65),

$$H_2O + e^- + * \rightarrow *H + OH^-\ (Volmer)$$

where* refers to the active site of the Pd (200) surface and *H depicts hydrogen intermediates adsorbed on the electrode surface.

Data, Materials, and Software Availability. All study data are included in the article and/or *SI Appendix*, thus, all the data have been deposited in a publicly accessible database.

ACKNOWLEDGMENTS. We acknowledge the National University of Singapore, Ministry of Education for their financial support, through the grants of A-0009176-02-00 and A-0009176-03-00, A*STAR (Agency for Science, Technology and Research) under its LCERFI program (Award No U2102d2002). L.W. would also like to acknowledge the support by National Research Foundation (NRF) Singapore, under NRF Fellowship (NRF-NRFF13-2021-0007). Computational work was performed using resources of the National Supercomputing Centre, Singapore.

Author affiliations: [a]Department of Chemical and Biomolecular Engineering, National University of Singapore, Singapore 117585, Singapore; [b]Department of Mechanical Engineering, National University of Singapore, Singapore 117575, Singapore; and [c]Institute of Sustainability for Chemicals, Energy and Environment, A*STAR, Jurong Island, Singapore 627833, Singapore

1. P. De Luna *et al.*, What would it take for renewably powered electrosynthesis to displace petrochemical processes? *Science* **364**, eaav3506 (2019).
2. O. S. Bushuyev *et al.*, What should we make with CO_2 and how can we make it? *Joule* **2**, 825–832 (2018).
3. K. Jiang *et al.*, Metal ion cycling of Cu foil for selective C-C coupling in electrochemical CO_2 reduction. *Nat. Catalysis* **1**, 111–119 (2018).
4. M. B. Ross *et al.*, Designing materials for electrochemical carbon dioxide recycling. *Nat. Catalysis* **2**, 648–658 (2019).
5. S. Gao *et al.*, Partially oxidized atomic cobalt layers for carbon dioxide electroreduction to liquid fuel. *Nature* **529**, 68–71 (2016).
6. C.-T. e. a. Dinh, CO_2 electroreduction to ethylene via hydroxide-mediated copper catalysis at an abrupt interface. *Science* **360**, 783–787 (2018).
7. X. Wang *et al.*, Mechanistic reaction pathways of enhanced ethylene yields during electroreduction of CO_2-CO co-feeds on Cu and Cu-tandem electrocatalysts. *Nat. Nanotechnol.* **14**, 1063–1070 (2019).
8. S. Chu, Y. Cui, N. Liu, The path towards sustainable energy. *Nat. Mater* **16**, 16–22 (2016).
9. K. K. Sakimoto, A. B. Wong, P. Yang, Self-photosensitization of nonphotosynthetic bacteria for solar-to-chemical production. *Science* **351**, 74–77 (2016).
10. Y. Wu, Z. Jiang, X. Lu, Y. Liang, H. Wang, Domino electroreduction of CO_2 to methanol on a molecular catalyst. *Nature* **575**, 639–642 (2019).
11. S. Verma, S. Lu, P. J. A. Kenis, Co-electrolysis of CO_2 and glycerol as a pathway to carbon chemicals with improved technoeconomics due to low electricity consumption. *Nat. Energy* **4**, 466–474 (2019).
12. M. Ma, K. Djanashvili, W. A. Smith, Controllable hydrocarbon formation from the electrochemical reduction of CO_2 over Cu nanowire arrays. *Angew Chem. Int. Ed Engl.* **55**, 6680–6684 (2016).
13. D. Wakerley *et al.*, Gas diffusion electrodes, reactor designs and key metrics of low-temperature CO_2 electrolysers. *Nat. Energy* **7**, 130–143 (2022).
14. J. M. Spurgeon, B. Kumar, A comparative technoeconomic analysis of pathways for commercial electrochemical CO_2 reduction to liquid products. *Energy Environ. Sci.* **11**, 1536–1551 (2018).
15. M. Jouny, W. Luc, F. Jiao, General techno-economic analysis of CO_2 electrolysis systems. *Ind. Eng. Chem. Res.* **57**, 2165–2177 (2018).
16. B. Ren *et al.*, Nano-crumples induced Sn-Bi bimetallic interface pattern with moderate electron bank for highly efficient CO_2 electroreduction. *Nat. Commun.* **13**, 2486 (2022).
17. L. Li *et al.*, Stable, active CO_2 reduction to formate via redox-modulated stabilization of active sites. *Nat. Commun.* **12**, 5223 (2021).

18. W. Ma *et al.*, Promoting electrocatalytic CO_2 reduction to formate via sulfur-boosting water activation on indium surfaces. *Nat. Commun.* **10**, 892 (2019).
19. G. Wen *et al.*, Orbital interactions in Bi-Sn Bimetallic electrocatalysts for highly selective electrochemical CO_2 reduction toward formate production. *Adv. Energy Mater.* **8**, 1802427 (2018).
20. L. Fan, C. Xia, P. Zhu, Y. Lu, H. Wang, Electrochemical CO_2 reduction to high-concentration pure formic acid solutions in an all-solid-state reactor. *Nat. Commun.* **11**, 3633 (2020).
21. S. He *et al.*, The p-orbital delocalization of main-group metals to boost CO_2 electroreduction. *Angew. Chem. Int. Ed Engl.* **57**, 16114–16119 (2018).
22. Z. Chen, K. Mou, S. Yao, L. Liu, Highly selective electrochemical reduction of CO_2 to formate on metal-free nitrogen-doped PC61BM. *J. Mater. Chem. A* **6**, 11236–11243 (2018).
23. Z. Chen, K. Mou, X. Wang, L. Liu, Nitrogen-doped graphene quantum dots enhance the activity of Bi_2O_3 nanosheets for electrochemical reduction of CO_2 in a wide negative potential region. *Angew Chem. Int Ed Engl.* **57**, 12790–12794 (2018).
24. C. Genovese *et al.*, Operando spectroscopy study of the carbon dioxide electro-reduction by iron species on nitrogen-doped carbon. *Nat. Commun.* **9**, 935 (2018).
25. X. Min, M. W. Kanan, Pd-catalyzed electrohydrogenation of carbon dioxide to formate: high mass activity at low overpotential and identification of the deactivation pathway. *J. Am. Chem. Soc.* **137**, 4701–4708 (2015).
26. B. Jiang, X. G. Zhang, K. Jiang, D. Y. Wu, W. B. Cai, Boosting formate production in electrocatalytic CO_2 reduction over wide potential window on Pd surfaces. *J. Am. Chem. Soc.* **140**, 2880–2889 (2018).
27. X. Yang, J. H. Lee, S. Kattel, B. Xu, J. G. Chen, Tuning reaction pathways of electrochemical conversion of CO_2 by growing Pd shells on Ag nanocubes. *Nano Lett.* **22**, 4576–4582 (2022).
28. R. Kortlever, I. Peters, S. Koper, M. T. M. Koper, Electrochemical CO_2 reduction to formic acid at low overpotential and with high faradaic efficiency on carbon-supported bimetallic Pd–Pt nanoparticles. *ACS Catal.* **5**, 3916–3923 (2015).
29. R. Lin *et al.*, PdAg bimetallic electrocatalyst for highly selective reduction of CO_2 with low COOH* formation energy and facile CO desorption. *Nano Res.* **12**, 2866–2871 (2019).
30. D. Gao *et al.*, Size-dependent electrocatalytic reduction of CO_2 over Pd nanoparticles. *J. Am. Chem. Soc.* **137**, 4288–4291 (2015).
31. S. Zhu *et al.*, Tuning structural and compositional effects in Pd-Au Nanowires for highly selective and active CO_2 electrochemical reduction reaction. *Adv. Energy Mater.* **8**, 1802238 (2018).
32. X. Chen, L. P. Granda-Marulanda, I. T. McCrum, M. T. M. Koper, How palladium inhibits CO poisoning during electrocatalytic formic acid oxidation and carbon dioxide reduction. *Nat. Commun.* **13**, 38 (2022).
33. J. Bok *et al.*, Designing atomically dispersed Au on tensile-strained Pd for efficient CO_2 electroreduction to formate. *J. Am. Chem. Soc.* **143**, 5386–5395 (2021).
34. B. M. Tackett, J. H. Lee, J. G. Chen, Electrochemical conversion of CO_2 to syngas with palladium-based electrocatalysts. *Acc. Chem. Res.* **53**, 1535–1544 (2020).
35. M. J. W. Blom, W. P. M. van Swaaij, G. Mul, S. R. A. Kersten, Mechanism and micro kinetic model for electroreduction of CO_2 on Pd/C: The role of different palladium hydride phases. *ACS Catal.* **11**, 6883–6891 (2021).
36. J. H. Lee *et al.*, Tuning the activity and selectivity of electroreduction of CO_2 to synthesis gas using bimetallic catalysts. *Nat. Commun.* **10**, 3724 (2019).
37. W. Sheng *et al.*, Electrochemical reduction of CO_2 to synthesis gas with controlled CO/H_2 ratios. *Energy Environ. Sci.* **10**, 1180–1185 (2017).
38. D. Gao *et al.*, Switchable CO_2 electroreduction via engineering active phases of Pd nanoparticles. *Nano Res.* **10**, 2181–2191 (2017).
39. H. Lv *et al.*, Single-crystalline mesoporous palladium and palladium-copper nanocubes for highly efficient electrochemical CO_2 reduction. *CCS Chem.* **4**, 1376–1385 (2022).
40. Y. Zhou *et al.*, Mesoporous PdAg nanospheres for stable electrochemical CO_2 reduction to formate. *Adv. Mater.* **32**, e2000992 (2020).
41. R. Zhou *et al.*, Two-dimensional palladium-copper alloy nanodendrites for highly stable and selective electrochemical formate production. *Nano Lett.* **21**, 4092–4098 (2021).
42. C. W. Lee, N. H. Cho, K. T. Nam, Y. J. Hwang, B. K. Min, Cyclic two-step electrolysis for stable electrochemical conversion of carbon dioxide to formate. *Nat. Commun.* **10**, 3919 (2019).
43. N. Han, P. Ding, L. He, Y. Li, Y. Li, Promises of main group metal-based nanostructured materials for electrochemical CO_2 reduction to formate. *Adv. Energy Mater.* **10**, 1902338 (2019).
44. J. Chen, L. Wang, Effects of the catalyst dynamic changes and influence of the reaction environment on the performance of electrochemical CO_2 reduction. *Adv. Mater.* **34**, e2103900 (2022).
45. W. Zheng, J. Qu, X. Hong, K. Tedsree, S. C. E. Tsang, Probing the size and shape effects of cubic- and spherical-shaped palladium nanoparticles in the electrooxidation of formic acid. *ChemCatChem* **7**, 3826–3831 (2015).
46. M. Luo *et al.*, Facile removal of polyvinylpyrrolidone (PVP) adsorbates from Pt alloy nanoparticles. *J. Mater. Chem. A* **3**, 2770–2775 (2015).
47. S. M. Ansar *et al.*, Removal of molecular adsorbates on gold nanoparticles using sodium borohydride in water. *Nano Lett.* **13**, 1226–1229 (2013).
48. M. Rahaman, A. Dutta, P. Broekmann, Size-dependent activity of palladium nanoparticles: Efficient conversion of CO_2 into formate at low overpotentials. *ChemSusChem* **10**, 1733–1741 (2017).
49. F. Zhou, H. Li, M. Fournier, D. R. MacFarlane, Electrocatalytic CO_2 Reduction to formate at low overpotentials on electrodeposited Pd Films: Stabilized performance by suppression of CO formation. *ChemSusChem* **10**, 1509–1516 (2017).
50. W. Zhu, B. M. Tackett, J. G. Chen, F. Jiao, Bimetallic Electrocatalysts for CO(2) Reduction. *Top Curr. Chem. (Cham)* **376**, 41 (2018).
51. Q. Lu, J. Rosen, F. Jiao, Nanostructured metallic electrocatalysts for carbon dioxide reduction. *ChemCatChem* **7**, 38–47 (2015).
52. A. Klinkova *et al.*, Rational design of efficient palladium catalysts for electroreduction of carbon dioxide to formate. *ACS Catal.* **6**, 8115–8120 (2016).
53. H. Dong *et al.*, Facet design promotes electroreduction of carbon dioxide to carbon monoxide on palladium nanocrystals. *Chem. Eng. Sci.* **194**, 29–35 (2019).
54. G. H. Han, S. H. Lee, M. G. Seo, K. Y. Lee, Effect of polyvinylpyrrolidone (PVP) on palladium catalysts for direct synthesis of hydrogen peroxide from hydrogen and oxygen. *RSC Adv.* **10**, 19952–19960 (2020).
55. X. Tan *et al.*, Polyvinylpyrrolidone- (PVP-) coated silver aggregates for high performance surface-enhanced Raman scattering in living cells. *Nanotechnology* **20**, 445102 (2009).
56. V. Muravev *et al.*, Interface dynamics of Pd–CeO2 single-atom catalysts during CO oxidation. *Nat. Catal.* **4**, 469–478 (2021).
57. X. Chen, L. P. Granda-Marulanda, I. T. McCrum, M. T. M. Koper, Adsorption processes on a Pd monolayer-modified Pt(111) electrode. *Chem. Sci.* **11**, 1703–1713 (2020).
58. J. R. J. K. Nørskov *et al.*, Origin of the overpotential for oxygen reduction at a fuel-cell cathode. *J. Phys. Chem. B* **108**, 17886–17892 (2004).
59. J. Fan *et al.*, Hydrogen stabilized RhPdH 2D bimetallene nanosheets for efficient alkaline hydrogen evolution. *J. Am. Chem. Soc.* **142**, 3645–3651 (2020).
60. J. Kim *et al.*, Theoretical and experimental understanding of hydrogen evolution reaction kinetics in alkaline electrolytes with Pt-based core-shell nanocrystals. *J. Am. Chem. Soc.* **141**, 18256–18263 (2019).
61. I. Ledezma-Yanez *et al.*, Interfacial water reorganization as a pH-dependent descriptor of the hydrogen evolution rate on platinum electrodes. *Nat. Energy* **2**, 17031 (2017).
62. E. L. Clark *et al.*, Explaining the incorporation of oxygen derived from solvent water into the oxygenated products of CO reduction over Cu. *J. Am. Chem. Soc.* **141**, 4191–4193 (2019).
63. M. He *et al.*, Oxygen induced promotion of electrochemical reduction of CO_2 via co-electrolysis. *Nat. Commun.* **11**, 3844 (2020).
64. M. Jin, H. Zhang, Z. Xie, Y. Xia, Palladium nanocrystals enclosed by 100 and 111 facets in controlled proportions and their catalytic activities for formic acid oxidation. *Energy Environ. Sci.* **5**, 6352–6357 (2012).
65. Y. Zheng, Y. Jiao, M. Jaroniec, S. Z. Qiao, Advancing the electrochemistry of the hydrogen-evolution reaction through combining experiment and theory. *Angew. Chem. Int. Ed Engl.* **54**, 52–65 (2015).